# Near- and Far-Field Observation of Phonon Polaritons in Wafer-Scale Multilayer Hexagonal Boron Nitride Prepared by Chemical Vapor Deposition

*Eugenio Calandrini, Kirill Voronin, Osman Balci, Maria Barra-Burillo, Andrei Bylinkin, Sachin M. Shinde, Subash Sharma, Fèlix Casanova, Luis E. Hueso, Andrei Chuvilin, Clifford McAleese, Ben R. Conran, Xiaochen Wang, Kenneth Teo, Valentyn S. Volkov, Andrea C. Ferrari, Alexey Y. Nikitin, and Rainer Hillenbrand\**

Polaritons in layered materials (LMs) are a promising platform to manipulate and control light at the nanometer scale. Thus, the observation of polaritons in wafer-scale LMs is critically important for the development of industrially relevant nanophotonics and optoelectronics applications. In this work, phonon polaritons (PhPs) in wafer-scale multilayer hexagonal boron nitride (hBN) grown by chemical vapor deposition are reported. By infrared nanoimaging, the PhPs are visualized, and PhP lifetimes of ≈0.6 ps are measured, comparable to that of micromechanically exfoliated multilayer hBN. Further, PhP nanoresonators are demonstrated. Their quality factors of ≈50 are about 0.7 times that of state-of-the-art devices based on exfoliated hBN. These results can enable PhP-based surface-enhanced infrared spectroscopy (e.g., for gas sensing) and infrared photodetector applications.

E. Calandrini, M. Barra-Burillo, A. Bylinkin, F. Casanova, L. E. Hueso, A. Chuvilin, R. Hillenbrand
CIC nanoGUNE BRTA
Tolosa Hiribidea, 76, Donostia–San Sebastián 20018, Spain
E-mail: r.hillenbrand@nanogune.eu

K. Voronin, A. Bylinkin, A. Y. Nikitin
Donostia International Physics Center (DIPC)
Paseo Manuel de Lardizabal, 4, Donostia–San Sebastián 20018, Spain

O. Balci, S. M. Shinde, S. Sharma, A. C. Ferrari
Cambridge Graphene Centre
University of Cambridge
9 JJ Thomson Ave, Cambridge CB3 0FA, UK

F. Casanova, L. E. Hueso, A. Chuvilin, A. Y. Nikitin, R. Hillenbrand
IKERBASQUE
Basque Foundation for Science
Bilbao 48009, Spain

C. McAleese, B. R. Conran, X. Wang, K. Teo
AIXTRON Ltd, Buckingway Business Park
Anderson Rd, Swavesey, Cambridge CB24 4FQ, UK

V. S. Volkov
XPANCEO
Bayan Business Center
DIP, Dubai 607-0406, UAE

## 1. Introduction

Polaritons are electromagnetic waves formed by the coupling of light to dipolar material excitations, such as plasmons, phonons, or excitons. They are at the center of an ever-growing research effort due to the possibility to confine and manipulate light at the nanometer scale. Layered materials (LMs) have opened new avenues for polariton-based nanophotonics.[1,2] Plasmon and phonon polaritons, for example in graphene[3] and polar materials such as hBN,[4] $\alpha$-MoO$_3$[5] and $\alpha$-V$_2$O$_5$,[6] respectively, can propagate with unpreceded short wavelengths and field confinement, long lifetimes and anomalous wavefronts.[1,2,7] They promise manifold future applications, such as ultrasensitive surface-enhanced infrared absorption (SEIRA) spectroscopy based on polariton resonators,[8–11] deep subwavelength-scale infrared waveguiding,[12,13] and ultrafast nanoscale heat transfer.[14,15]

Most LM polariton experiments so far rely on the micromechanical exfoliation of individual flakes from their bulk crystals, which is not sufficient for efficient and scalable fabrication of polariton-based sensors and devices. Synthesis of millimeter-scale LMs is thus of critical importance, since they will offer the advantages of, for example, i) fabricating large-scale polariton nanoresonator arrays to improve the signal-to-noise ratio and thus the sensitivity in SEIRA applications, ii) superior control of layer thicknesses and their homogeneity, and iii) scalable and reproducible fabrication of large amounts of structures and devices, which will be a prerequisite for implementing LM polaritonics into real-world applications. Large-scale graphene layers can be already grown in good quality by chemical vapor deposition (CVD)[16] and plasmonic applications such as SEIRA spectroscopy[8,17,18] and plasmon-assisted infrared photodetection[19] have been already demonstrated. The large-scale growth of other LMs, however, is still in its infancy, particularly that of polar LMs hosting phonon polaritons (PhPs) that outperform graphene plasmons because of their much larger lifetimes (up to 8 ps[5]). Only recently, high-quality PhP resonators based on bottom-up synthesis were demonstrated with
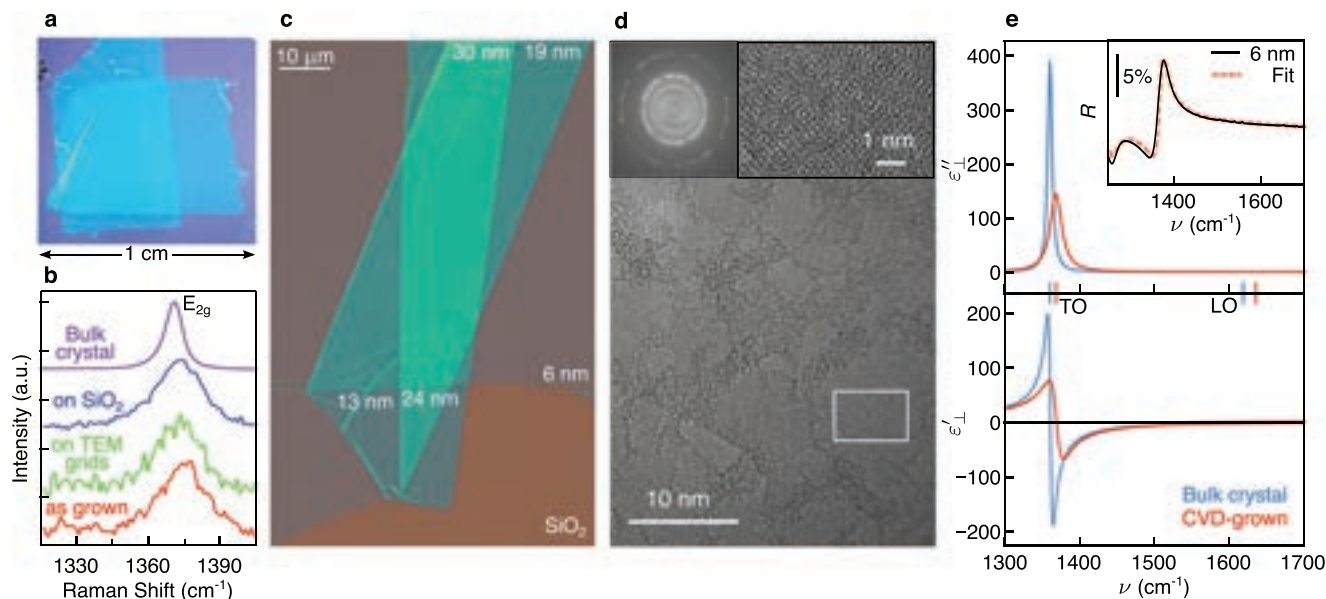
**Figure 1.** Structural and optical characterization of ML-hBN. a) Photograph of two centimeter-scale hBN multilayers transferred onto a $1 \times 1\,cm^2$ $SiO_2$/Si substrate. b) Raman spectra of as-grown and transferred CVD ML-hBN (acquired at 514.5 nm laser wavelength) and ME-hBN as reference.[26,27] c) Light microscopy image of a 6 nm-thick layer that was folded during the transfer onto a Si/SiO₂ substrate. The numbers indicate the respective total layer thickness (measured by AFM). d) TEM image of 1 nm-thick ML-hBN. Top right inset: Enlarged view of the area marked by the small white square in the center of the image. Top left inset: FT of the image. e) The red curves show the real (bottom) and imaginary (top) parts of the infrared in-plane component of the dielectric tensor of the ML-hBN, obtained by fitting the infrared reflection spectrum (inset) of a 6 nm-thick ML-hBN. For comparison, the blue curves show the same quantities measured for hBN crystals.[28]

chemically synthesized $MoO_3$ ribbons of 120 nm thickness[20] and PhP propagation was reported on millimeter-scale free-standing SiC membranes.[21] However, PhPs on large-scale films of LMs of several nanometer thicknesses have not been reported so far but are needed for the integration of LM-based PhP devices into CMOS-compatible fab-process lines.

CVD-growth of high-quality, large-scale polar LMs has been reported,[22–24] however, PhPs have been observed only in CVD-grown mono-, bi-, and trilayers hBN,[25] where the PhP wavelengths and propagation lengths are short, challenging the development of PhP-based resonators and devices. For this reason, the growth of large-scale multilayer hBN (ML-hBN) with thicknesses of several nanometers is critically important for the fabrication of larger resonator structures and to increase the coupling efficiency between light and LM phonon polariton resonators (as the scattering cross sections scale with the resonator volume).

Here, we report wafer-scale ML-hBN, up to 24 nm-thick, supporting PhPs with lifetimes of ≈0.6 ps. We verify the PhPs via polariton interferometry using scattering-type scanning near-field optical microscopy (s-SNOM). Random PhP interference patterns are observed, which we explain by PhP scattering at randomly distributed defects. By analysis of these patterns, we measure the PhP dispersion, propagation lengths, and lifetimes. All of them agree well with calculations based on the dielectric function of the ML-hBN, which was obtained from far-field infrared reflection spectroscopy. Our results show that PhP scattering at the defects does not have a significant influence on the PhP dispersion and damping. Consequently, Fabry–Pérot PhP nanoresonators, fabricated from ML-hBN exhibit remarkable quality fac-

tors of $Q \approx 50$, approaching that of PhP nanoresonators made of micromechanically exfoliated hBN (ME-hBN).

## 2. Results

Large-scale ML-hBN was grown on sapphire in an AIXTRON CCS 2D reactor (https://www.aixtron.com/en) as described in the Experimental Section. **Figure 1**a shows a photograph of two ML-hBN layers that were transferred onto a $SiO_2$/Si substrate (see Experimental Section), demonstrating that centimeter-scale layers can be obtained and stacked uniformly. The thickness and roughness (root mean square (RMS)) of the transferred ML-hBN are ≈5.5 and 0.9 nm, respectively, as measured from atomic force microscopy (AFM) images such as the ones shown in **Figure 2**b. A closer inspection with a light microscope (Figure 1c) of a similar sample reveals that ML-hBN can be folded multiple times, showing that the preparation of several 10 nm-thick layers can be achieved by stacking ML-hBN.

Figure 1b shows the Raman spectra of ML-hBN. For the as-grown material on the sapphire substrate, we observe a peak at 1371 cm⁻¹ (red curve) that shifts to 1368 cm⁻¹ after the transfer onto either Si/$SiO_2$ substrates or TEM grids (blue and green curves, respectively), indicating the relaxation of strain generated during the growth process. This peak is blueshifted by ≈2 cm⁻¹ with respect to the $E_{2g}$ Raman mode of hBN bulk crystals (purple curve).[26,27] On the other hand, the full-width at half-maximum (FWHM) of ≈20 cm⁻¹ is twice that of bulk hBN, which we attribute to structural imperfections and polycrystallinity, as confirmed by transmission electron microscopy (TEM). We observe domains, which exhibit moiré-like superlattices with different
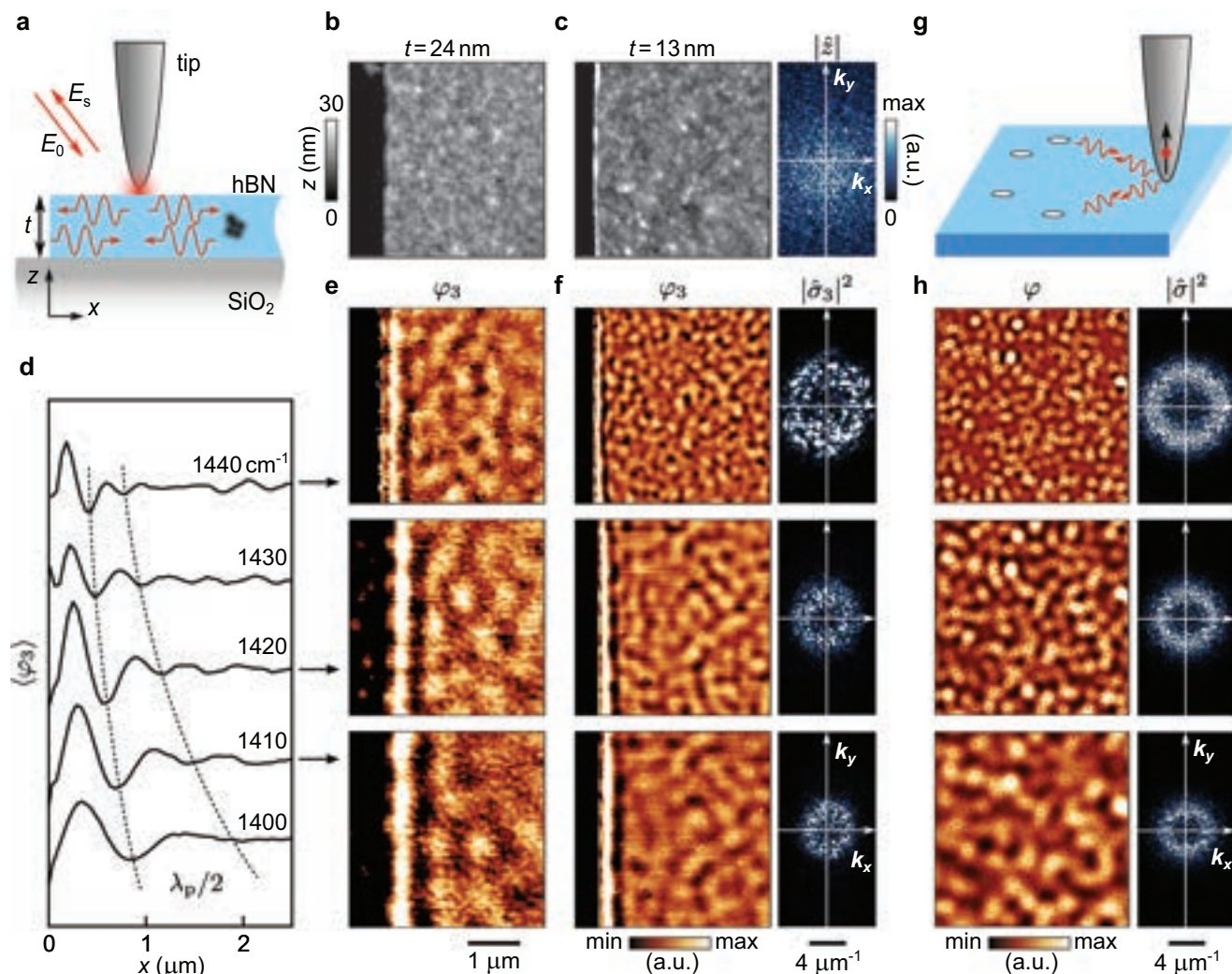
**ADVANCED
SCIENCE NEWS**

www.advancedsciencenews.com

**ADVANCED
MATERIALS**

www.advmat.de

**Figure 2.** Phonon polariton interferometry of ML-hBN. a) Schematic of the experiment. $E_0$ and $E_s$ denote the electric field of the incident and tip-scattered radiation. b,c) Topography images of the 24 nm- and 13 nm-thick ML-hBN. The right image in (c) shows the FT of the topography image of the 13 nm-thick ML-hBN. d) Averaged near-field phase line profiles extracted from (e) perpendicular to the ML-hBN edge. $x = 0$ μm corresponds to the ML-hBN edge. The dashed lines are guides to the eye, tracing adjacent signal minima. e,f) Near-field phase images $\varphi_3(x,y)$ of the 24 nm and 13 nm ML-hBN recorded at 1440, 1420, and 1410 cm$^{-1}$ (top to bottom). Right images of (f): FT of the complex-valued near-field images, $|\hat{\sigma}_3(k_x,k_y)|^2$. g) Schematic of the dipole model for simulating s-SNOM images. A point dipole source (black arrow) and randomly distributed holes (white dots) mimic the AFM tip and the defects in ML-hBN. h) Simulated phase images $\varphi(x,y)$ and FTs of the corresponding complex-valued s-SNOM images, $|\hat{\sigma}(k_x,k_y)|^2$.

crystal orientations due to the stacking of polycrystalline 1L-hBN (Figure 1d). Fast Fourier transform of the TEM image (top left inset in Figure 1d) shows rings confirming that our ML-hBN is polycrystalline (see Supporting Information). The top right inset in Figure 1d is the enlarged view of the white square in Figure 1e and shows the moiré-like superlattice in an individual domain. The dark boundaries are due to irregular stacking of 1L-hBN on each other, also indicating polycrystallinity. From the size of the moiré-like domains in Figure 1d we estimate a grain size in the range of 2 to 15 nm.

For measuring the in-plane component of the ML-hBN dielectric tensor, $\varepsilon_\perp(\nu)$, we performed far-field infrared reflection spectroscopy of a 6 nm-thick ML-hBN on a SiO$_2$/Si substrate (see Experimental Section). Fitting the reflection spectrum (inset of Figure 1e) by the Fresnel reflection coefficient describing the

ML-hBN/SiO$_2$/Si stack (see Experimental Section), we extracted the real and imaginary parts of $\varepsilon_\perp(\nu)$, $\varepsilon_\perp'(\nu)$ and $\varepsilon_\perp''(\nu)$, which are shown in Figure 1e (red curves). For comparison, we show the in-plane component of the dielectric tensor of a layer that was exfoliated from a crystal of naturally abundant hBN (blue curves).[28] Such a comparison is justified because i) the dielectric function of thin hBN layers is the same as that of bulk hBN crystals, even in the few monolayer limit,[29] and ii) the bulk dielectric function of hBN is typically used to quantitatively describe the dispersion of PhPs in thin exfoliated hBN layers.[4,28] For the CVD-grown layer, we find transversal optical (TO) and longitudinal optical (LO) phonon frequencies at 1369 and 1621 cm$^{-1}$, respectively, which are blueshifted ≈8 cm$^{-1}$ compared to that of ME-hBN, corroborating that the CVD-grown layer is hBN. On the other hand, the damping (according to $\varepsilon_\perp''(\nu)$) is a factor of about two larger
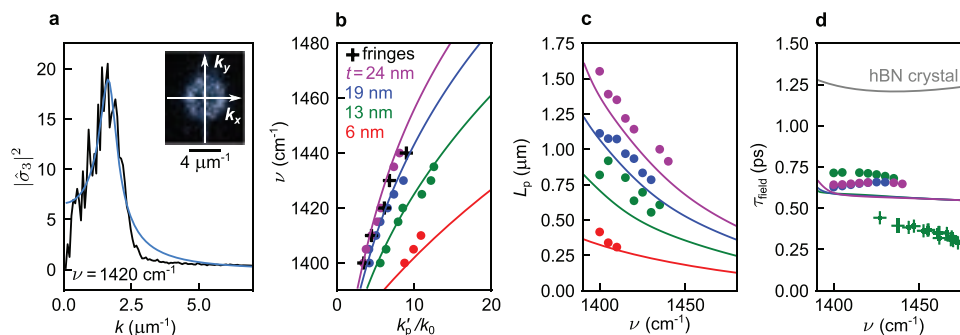
**Figure 3.** Comparison of measured and calculated PhP properties. a) The black curve shows radially averaged FT of the complex-valued s-SNOM image of a 19 nm-thick ML-hBN at 1420 cm$^{-1}$. The blue curve shows the fit by Equation (1). The inset shows $|\hat{\sigma}_3 (k_x, k_y)|^2$. b,c) PhPs dispersion and propagation length for stacked ML-hBNs of different total thicknesses $t$. The dots show results obtained from fitting the FTs of the various complex-valued s-SNOM images, analog to (a). The solid lines show the calculated PhP dispersions using the dielectric function of the ML-hBN shown in Figure 1e. The black crosses show the PhP dispersion obtained for the 24 nm-thick ML-hBN (Figure 2d) by measuring the spacing of the interference fringes parallel to the edge. d) Calculated (colored lines) and measured (dots; obtained from (b) and (d) as $\tau_{field} = L_p / \nu_g$) PhP lifetimes. Gray: Calculated PhP lifetime in a 13 nm-thick ME-hBN.[28]

for ML-hBN (consistent with the Raman spectroscopy results of Figure 1b), which we attribute to the nanocrystalline structure of the layer and growth defects.

The negative real part of $\varepsilon_\perp (\nu)$ between the TO and LO, frequencies indicates that this material can support PhPs. We explore this possibility by polariton interferometric nanoimaging of single and stacked ML-hBNs with a scattering-type s-SNOM.[30] As illustrated in Figure 2a, the metalized tip of an AFM is illuminated by a p-polarized infrared laser beam. The tip acts as an infrared nanoantenna that concentrates the incident field at its sharp apex, yielding a nanoscale near-field spot for launching the polaritons. The tip-launched polaritons propagate away from the tip and are typically reflected at layer edges and defects. Pseudo-heterodyne interferometric recording of the tip-scattered field as a function of tip position $(x, y)$ subsequently yields amplitude and phase images, $s_3(x, y)$ and $\varphi_3(x, y)$, which exhibit polariton interference fringes with a spacing of half the polariton wavelength, $\lambda_p / 2$ (see Experimental Section).[4,31,32]

Figure 2b,c show the topography images of 24 nm- and 13 nm-thick samples (4 and 2 stacked ML-hBNs, respectively), revealing homogeneous layers with a roughness of $\approx 2.7$ nm (RMS). In the infrared s-SNOM phase images $\varphi_3$ of the same areas, we observe strong signal fluctuations for all the investigated layers. This contrasts with infrared s-SNOM images of ME-hBN, where the interior of the flakes appears homogeneous and PhP interference fringes are observed only close to the edges and parallel to them.[25,32] Interestingly, the periodicity of the signal fluctuations increases with decreasing wavenumber, $\nu$, and with increasing layer thickness, which lets us assume that the infrared s-SNOM pattern is the consequence of PhP interference caused by scattering of PhPs at randomly distributed defects all over the ML-hBN. Our interpretation is supported by the appearance of fringes parallel to the edge of the ML-hBN, whose spacing exhibits the same behavior. From the line profiles shown in Figure 2d (extracted from the infrared images of the 24 nm-thick ML-hBN perpendicular to the edge and averaged over 128 lines), we can directly measure the PhP wavelengths, as one signal oscillation period corresponds to $\lambda_p / 2$. Measurements for different $\nu$ yield the PhP dispersion (black crosses in **Figure 3**b), which matches well the po-

lariton dispersion calculated for a 24 nm-thick layer on a SiO$_2$/Si substrate with a dielectric function (red curves in Figure 1e) corresponding to that of the CVD ML-hBN (see Experimental Section).

For the ML-hBNs thinner than 24 nm, we barely observe interference fringes parallel to the edge. Further, they are strongly distorted by random PhP interference patterns. This prevents the direct measurement of the PhP wavelength from the spacing of the fringes parallel to the ML-hBN edges. We thus analyze the random interference pattern (yielding the same PhP properties as the analysis of fringes parallel to the ML-hBN edges, as verified in Figure 3b) via Fourier transform (FT) of the s-SNOM images. Because of the short PhP propagation lengths, it is critically important to perform a complex-valued FT of the complex-valued s-SNOM images, $\sigma_3(x, y) = s_3(x, y) e^{i\varphi_3(x, y)}$, rather than an FT of phase $\varphi_3(x, y)$ or amplitude $s_3(x, y)$ images only (Supporting Information).[33] Figure 2f shows $|\hat{\sigma}_3(k_x, k_y)|^2 = |\mathcal{F}[\sigma_3(x, y)]|^2$ of the complex-valued s-SNOM images of the 13 nm-thick ML-hBN. A bright ring is observed (in contrast to the FT of the topography image in Figure 2c), revealing a well-defined isotropic periodicity of the pattern observed in the near-field images. Importantly, the diameter of the ring increases $\nu$, thus indicating PhPs that propagate in all directions.

To verify our interpretation and to establish a quantitative analysis of the FT to measure the PhP dispersion, we developed an analytical model. Considering that the thickness of the ML-hBN is much smaller than the polariton wavelength, the sample is described by a conductive sheet[34,35] (on a SiO$_2$/Si substrate) with the dielectric function shown by the red curves in Figure 1e, which contains randomly distributed PhP scatterers (illustrated in Figure 1g). The tip is modeled as a point dipole source launching PhPs and we consider only single scattering events at the nearest scatterers. The total complex-valued electric field below the dipole source, mimicking the s-SNOM signal, is calculated as a function of the dipole position, $\sigma(x, y) = s(x, y) e^{i\varphi(x, y)}$ (see Experimental Section). For a PhP scatterer density of 30 µm$^{-2}$ and a layer thickness of 13 nm, the calculated phase images $\varphi(x, y)$ and FT $|\hat{\sigma}(k_x, k_y)|^2 = |\mathcal{F}[\sigma(x, y)]|^2$ match well the experimental results of Figure 2f, supporting our assumption that the IR near-field

pattern stems from propagating PhPs scattering at randomly distributed defects. The model allows us to derive an analytical expression for fitting $|\hat{\sigma}(k)|^2$ according to:

$$|\hat{\sigma}(k)|^2 \propto \frac{1}{\sqrt{\left(k^2 - 4\left[\left(k'_p\right)^2 - \left(k''_p\right)^2\right]\right)^2 + 64\left(k'_p\right)^2\left(k''_p\right)^2}} \quad (1)$$

where $k = \sqrt{k_x^2 + k_y^2}$ and the complex-valued polariton momentum $k_p = k'_p + ik''_p$ is the only fitting parameter describing the single mode supported by the layer, that is, the M0 mode (see Experimental Section and Supporting Information).

Figure 3a shows, by way of an example, the fitting (blue curve) of a radially averaged FT of the complex-valued s-SNOM image (black curve) of a 19 nm-thick ML-hBN at 1420 cm$^{-1}$. Analogous fitting of the complex-valued s-SNOM images of one- to fourfold stacked ML-hBN) yields the PhP dispersions $\nu(k'_p)$ shown in Figure 3b (dots). Comparing the PhP dispersion for the 24 nm ML-hBN (purple dots) with that obtained from the spacing of the interference fringes (black crosses, described above), we find excellent agreement between the two measurements, validating the dispersion measurement via fitting the FT of the complex-valued s-SNOM images by Equation (1).

From the fitting to the radially averaged FTs of the complex-valued s-SNOM images we also obtained the imaginary part of the polariton wavevectors, $k''_p$, yielding PhP propagation lengths $L_p = 1/k''_p$ and lifetimes $\tau_{field} = L_p/v_g$, where $v_g = d\omega/dk'_p$ is the group velocity and $\omega$ the angular frequency (dots in Figure 3c,d, respectively). Altogether, the results reveal the typical behavior of PhPs: i) the wavevector $k'_p$ increases as the wavenumber increases and the thickness decreases (Figure 3b), ii) the propagation length $L_p$ decreases with increasing wavenumber and decreasing thickness (Figure 3c), and iii) the lifetime $\tau_{field}$ is independent of wavenumber and thickness (Figure 3d). Importantly, $\tau_{field}$ of ≈0.6 ps is only a factor of about two smaller than the PhP lifetime in high-quality hBN (indicated by the gray solid curve in Figure 3d).

For comparison, we calculated the PhP dispersions, propagation lengths, and lifetimes using the dielectric function of hBN shown in Figure 1e (solid lines in Figure 3b,d; see Experimental Section). A good agreement between experiment and theory is found for all ML-hBN thicknesses, corroborating that the random fringe patterns reveal propagating PhPs that seem to randomly scatter at nanoscale defects. Further, it shows that the dielectric function of the ML-hBN obtained by far-field reflection spectroscopy reveals the optical material properties between the PhP scattering centers where the PhPs propagate. Thus, the PhP scattering centers do not significantly influence the macroscopic dielectric function and we conclude that the increased phonon damping as compared to ME-hBN flakes stems from homogenously distributed atomic-scale defects, revealed by TEM (Figure 1b). To test the reproducibility of our PhP observations, we recorded s-SNOM images of two further samples (see Figure S6, Supporting Information), with ML-hBN grown in separate CVD processes. In the s-SNOM images of these samples, we observed again the random PhP interference patterns, from which we determined the PhP wavevectors. These wavevec-

tors agree well with calculated PhP wavevectors using the dielectric function shown in Figure 1e, thus demonstrating the reproducibility of the ML-hBN layer growth and PhP properties (Section S7, Supporting Information).

We finally explore the possibility to fabricate PhP nanoresonators from ML-hBN, which could be applied for SEIRA spectroscopy[9] or gas sensing.[36] In **Figure 4** we show far- and near-field IR spectroscopy (illustrated in Figure 4a,f) of ribbons arrays fabricated by e-beam lithography and reactive-ion etching (RIE) of a 13 nm-thick ML-hBN obtained by stacking two individual CVD ML-hBN (Experimental Section). Owing to the large-scale homogeneous ML-hBN layers, we could fabricate 30 arrays of $40 \times 40$ μm$^2$, allowing for systematic variation of the ribbon width $w$. The far-field reflection spectra (Experimental Section) of the ribbon arrays show peaks that shift to higher wavenumbers as the ribbon width $w$ decreases (Figure 4b), thus indicating PhP resonances.[9,10] Simulations for the far-field reflection spectra (Experimental Section) employing the dielectric function of ML-hBN (shown in Figure 1e) reproduce well the experimental reflection spectra. We first elucidate the spatial distribution of the resonating PhP mode by s-SNOM imaging of the 156 nm-wide ribbons near their resonance peak at 1450 cm$^{-1}$ (Figure 4g). We find a strong near-field amplitude signal $s_3$ at the ribbon edges and a rather weak signal in the ribbon center, which corresponds to a strong near-field concentration at the ribbon edges. The resonance can be thus attributed to a dipolar mode, which is confirmed by the calculated spatial near-field distribution across one ribbon shown in Figure 4h. The near-field signal variations along the ribbon edges in the s-SNOM image can be attributed to local variations in the ribbon width, polycrystallinity of CVD ML-hBN, and fabrication damage.

To quantify and interpret the dipolar modes, we extracted for each ribbon array the resonance wavenumber $\nu_{res}$ and linewidth $\Delta\nu$. To that end, we fitted a Fano lineshape (red dotted curves in Figure 4b,c) to the measured and simulated spectra (black curves in Figure 4b,c) to account for the peak asymmetry, due to the interference between light scattered at the ribbons and reflected at the SiO$_2$/Si surface (see Experimental Section). An excellent fitting is achieved. From the dipolar near-field distribution observed in Figure 4g, we assume that the peaks correspond to the first-order Fabry–Pérot PhP resonance of the fundamental PhP mode (typically referred to as the M0 mode). We can attribute then a PhP wavevector $k_{res} = (\pi - \theta)/w$ to each resonance, where $\theta = 0.32\pi$ is the PhP reflection phase at the ribbon edges (see Supporting Information) and $w$ is the ribbon width, which was measured by scanning electron microscopy (SEM). In Figure 4d we show $\nu_{res}(k_{res})$ obtained from the measured (green crosses) and simulated spectra (blue dots). They agree well with each other and the positions of the spectral maxima match the calculated PhP dispersion (black solid line) for an unstructured ML-hBN with the dielectric function shown in Figure 1e, confirming that the resonances are caused by PhP modes propagating forth and back transversely to the ML-hBN ribbons. From the materials science perspective, the remarkable match between calculated and measured PhP dispersions in Figure 4d demonstrates that the CVD growth process yields ML-hBN layers of homogeneous thickness and dielectric function on the millimeter-scale, since the individual ribbon arrays are distributed over an area of ≈$0.5 \times 0.5$ mm$^2$.
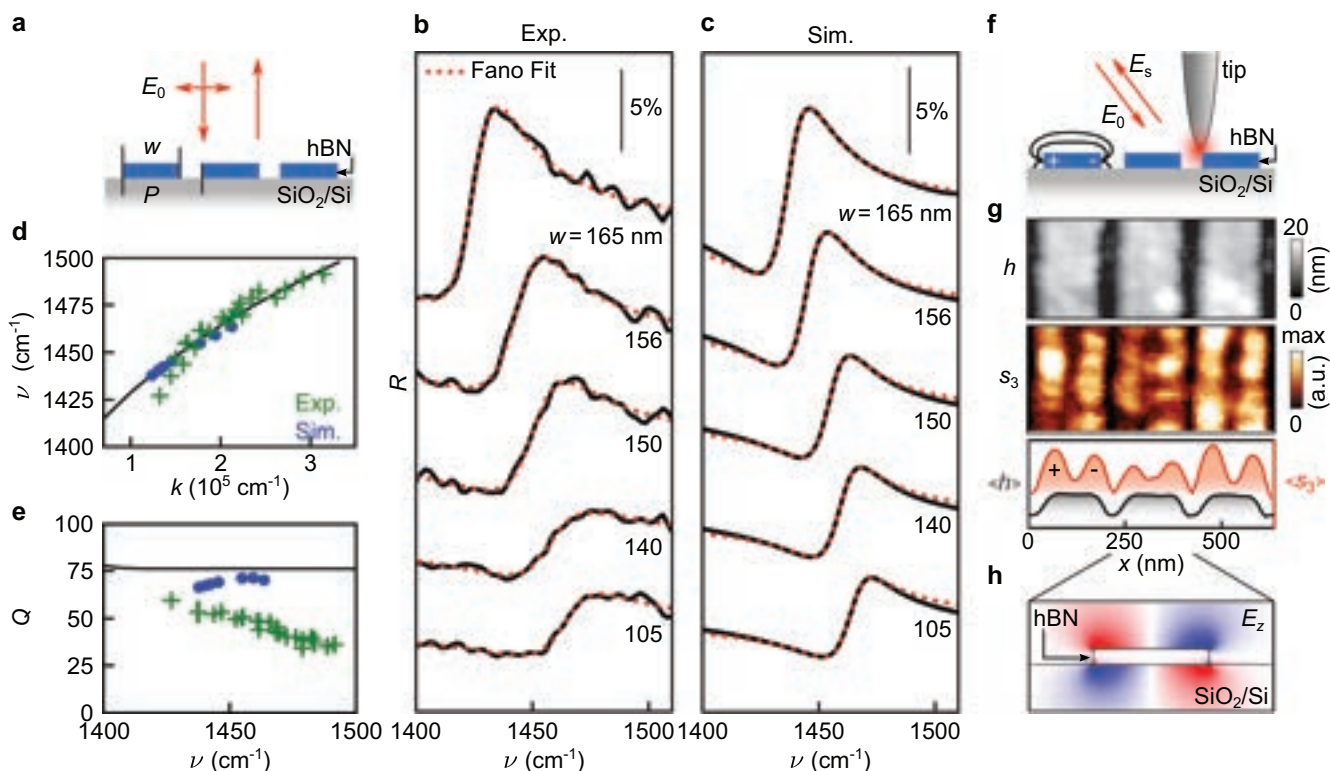
**Figure 4.** Far- and near-field characterization of ribbons fabricated from a 13 nm-thick ML-hBN. a) Schematic of far-field infrared reflection spectroscopy experiment. b,c) Black curves: Measured and simulated reflection spectra of ML-hBN ribbon arrays of different $w$. Red dashed lines: Fits with Fano line shapes. d) Green crosses and blue dots: PhP dispersions obtained from Fano fits of measured and simulated reflection spectra, respectively, and assuming Fabry–Pérot resonances transverse to the ribbons (Experimental Section). Black curve: Calculated PhP dispersion (Experimental Section) for a 13 nm ML-hBN with the dielectric function shown in Figure 1e. e) Quality factors of the ribbon resonances obtained from the Fano fits of the measured (green crosses) and simulated (blue dots) ribbon resonances. Black curve: Calculated $Q$ from calculated lifetime in Figure 3d. f) Schematic of the near-field imaging experiment. g) Topography (showing height $h$, top) and near-field amplitude ($s_3$, center) images of $w = 156$ nm-wide ML-hBN ribbons near the resonance wavenumber $\nu$ (1450 cm$^{-1}$). The bottom graph shows averaged topography and near-field amplitude line profiles across the ribbons. h) Simulated cross section of the electric near-field distribution (vertical field component $E_z$) of a single ML-hBN ribbon with $w = 156$ nm.

From the linewidths $\Delta \nu$ we determined the quality factor of the resonances according to $Q = \omega_{res}/\Delta\omega = \nu_{res}/\Delta\nu$. The experimental $Q$ (green crosses in Figure 4e) decreases from $\approx 60$ to 30 with decreasing ribbon width $w$, while the estimated $Q$ from the simulated spectra is $\approx 70$ (blue dots in Figure 4e). We explain the reduced experimental $Q$ by additional PhP damping due to fabrication-induced damage and roughness at the ribbon edges, similar to what has been reported for PhP resonances in ribbons made of ME-hBN.[9] We also show in Figure 4e the theoretical limit, $Q_{lim} = \omega\tau = 2\pi c \nu \tau$ (black line), where $\tau = 1/\Delta\omega$ is the theoretical limit of the PhP lifetime according to $\tau = \tau_{field}/2$ with $\tau_{field} = L_p/\nu_g$ (blue curve in Figure 3d). Note that $\tau$ in standard far-field spectroscopy defines the time in which the intensity of an excitation decays to $1/e$ of its initial value, implying that $\tau = \tau_{field}/2$.[37] We obtain a $Q_{lim}$ of $\approx 77$, slightly larger than the estimated $Q$ from the simulated ribbon spectra, revealing that the damping of the simulated PhP resonances is dominated by PhP dissipation (governed by the imaginary part of the dielectric function of ML-hBN) rather than by radiation losses. We note that the rather large quality factors seem to contradict the short relative PhP propagation lengths, that is, the observation of only a few polariton fringes near the hBN edges in the s-SNOM images

shown in Figure 2. To clarify this issue, we express the relative polariton propagation length, $L_p/\lambda_p$, as a function of $Q$:[33]

$$\frac{L_p}{\lambda_p} = \frac{k'_p}{2\pi k''_p} = \frac{1}{\pi}\frac{\nu_g}{c}qQ \qquad (2)$$

where $q = k'_p/k_0$ with $k_0$ being the wavevector of the photon. We find that $L_p/\lambda_p$ does not only scale with $Q$ but also with the group velocity $\nu_g$, which for PhPs in thin layers is typically two or three orders of magnitude smaller than $c$.[38] Thus, we obtain $L_p/\lambda_p \approx 1$ for PhPs at 1435 cm$^{-1}$ and an hBN layer thickness of 13 nm, where $q = 12.6$ and $\nu_g = 3.24 \times 10^{-3}\,c$. This quite short relative propagation length is fully consistent with the few PhP fringes observed in Figure 2f.

## 3. Conclusion

We have employed IR nanoimaging to demonstrate that millimeter-sized ML-hBN of 6 nm thickness can support, individually or when stacked, PhPs with lifetimes up to 0.6 ps, being only a factor of two reduced compared to that of phonon

**2302045 (6 of 9)**

**ADVANCED
SCIENCE NEWS**

www.advancedsciencenews.com

**ADVANCED
MATERIALS**

www.advmat.de

polaritons in high-quality ME-hBN flakes. On the other hand, IR nanoimaging showed random PhP interference patterns, which could be explained by the presence of defects acting as PhP scatterers that are not recognized by other techniques, such as far-field infrared spectroscopy, or SEM and TEM. Thus, the analysis of PhP interference patterns may become a valuable method of quality assessment of CVD-grown 2D materials and for studying growth defects. Artificial intelligence may be applied to analyze the s-SNOM images,[39–41] based on a training of a neural network with simulated polariton interference patterns (according to the model presented in this work) obtained for different defect distributions. Despite strong PhP scattering, our ML-hBN allows the fabrication of Fabry–Pérot phonon polariton resonators with quality factors up to $Q \approx 50$, demonstrating the potential of ML-hBN for large-scale fabrication of PhP nanoresonators for infrared gas sensing[36] and phonon–polariton-assisted detection of infrared radiation.[42]

## 4. Experimental Section

*CVD Growth of hBN Layers*:  ML-hBN was grown on c-plane $Al_2O_3$ (0001) at 1400 °C, 500 mbar for 30 mins in an AIXTRON CCS 2D reactor. Borazine was used as a precursor, with 10 sccm $N_2$ to transport it. Prior to hBN growth, the substrate was annealed in $H_2$ for 10 mins at 150 mbar and 1200 °C. ML-hBN was then wet transferred on $SiO_2/Si^+$ (285 nm/500 μm) substrates and TEM grids.

*Transfer of ML-hBN*:  ML-hBN was spin-coated with poly(methyl methacrylate) (PMMA) A4 950 at 1000 rpm for 1 min and baked at 80 °C for 10 mins. The PMMA-coated ML-hBN on sapphire was kept in 8% $H_3PO_4$ for $\approx$10 h to delaminate it. The delaminated PMMA/hBN was kept in deionized (DI) water for 1–2 h. For the transfer on $SiO_2/Si$, the cleaned PMMA/hBN in DI water was scooped out with $SiO_2/Si$ and left drying for >5 h. The PMMA/hBN on $SiO_2/Si$ was baked at 80 °C for 10 mins and soaked in acetone and isopropyl alcohol (IPA) to remove the PMMA. To transfer another ML-hBN on a transferred ML-hBN on $SiO_2/Si$, the same procedure was followed, but PMMA/ML-hBN was scooped out with $hBN/SiO_2/Si$. To transfer ML-hBN on TEM grids, these were fixed on a glass slide with tape and the already delaminated and cleaned PMMA/ML-hBN in DI water was scooped out with the TEM grid on glass and left drying for >5 h. The PMMA/ML-hBN on the TEM grid/glass was baked at 80 °C for 10 mins and soaked in acetone and IPA to remove the PMMA.

*Raman Spectroscopy of hBN Layers*:  As grown and transferred ML-hBN was characterized by Raman spectroscopy with a Renishaw InVia instrument equipped with a 100× objective and illumination at 514.5 nm wavelength. A statistical analysis of 8 spectra on as-grown ML-hBN on sapphire, 6 on ML-hBN on TEM grids, 12 on $\approx$6 nm-thick ML-hBN on $SiO_2/Si$, and 10 on $\approx$13 nm-thick ML-hBN on $SiO_2/Si$ was performed to find the position (Pos) and FWHM of the ML-hBN $E_{2g}$ peak.[26] The errors were calculated from the standard deviation across different spectra and the spectrometer resolution of $\approx$1 cm$^{-1}$. Pos($E_{2g}$) 1371 $\pm$ 1 cm$^{-1}$ was found for the as-grown ML-hBN on sapphire and 1368 $\pm$ 1 cm$^{-1}$ for the 1 nm-thick ML-hBN transferred on TEM grid, 6 nm-thick ML-hBN and 13 nm-thick ML-hBN transferred on $SiO_2$. FWHM($E_{2g}$) = 20 $\pm$ 2 cm$^{-1}$, 19 $\pm$ 1 cm$^{-1}$, 21 $\pm$ 2 cm$^{-1}$, and 20 $\pm$ 2 cm$^{-1}$ was found for the corresponding linewidths.

*Far-Field FTIR Reflection Spectroscopy of hBN Layers and Ribbons*:  Reflection spectra of the ML-hBN (example shown in the inset of Figure 1e) were recorded with a Bruker Hyperion 2000 infrared microscope (Bruker Optics GmbH, Ettlingen, Germany) equipped with a 15× Cassegrain objective and coupled to a Bruker Vertex 70 FTIR spectrometer (Bruker Optics GmbH, Ettlingen, Germany). The spectra of the sample were normalized to the reflection spectrum of a gold mirror. The spectra of the ribbon arrays were measured with linear polarization (using a wire grid polarizer) perpendicular to the ribbons and normalized to the reflection spectrum of the clean $Si/SiO_2$ substrate. The spectral resolution was set to 2 cm$^{-1}$.

*Dielectric Functions of ML-hBN, SiO$_2$, and Si from Far-Field FTIR Reflection Spectra*:  A multilayer model was used based on the complex-valued Fresnel formulas[43] to fit the reflection spectra of the bare $SiO_2/Si$ substrate and the ML-hBN/$SiO_2/Si$ sample. Specular reflection with an incident angle of 17° was considered. The dielectric functions were used as fit parameters. First, the dielectric function of $SiO_2$ and Si was determined from the reflection spectra of the bare $SiO_2/Si$ substrate, which was described as a 285 nm-thick $SiO_2$ layer on a semi-infinite Si bulk material. The dielectric function of $SiO_2$ was modeled with two Lorentz oscillators and the free carriers in the Si substrate were described via the Drude model according to:

$$\varepsilon_{SiO_2}(\nu) = \varepsilon_{SiO_2,\infty} + \sum_{k=1,2} \frac{S_k \nu_k^2}{\nu_k^2 - \nu^2 - i\nu\Gamma_k} \tag{3}$$

$$\varepsilon_{Si}(\nu) = \varepsilon_{Si,\infty} - \frac{\nu_p^2}{\nu^2 - i\nu\Gamma_p} \tag{4}$$

where $\varepsilon_{k,\infty}$ are the high-frequency permittivity of Si and $SiO_2$, and the parameters $S_k$, $\nu_i$ and $\Gamma_k$ are the oscillator strengths, frequencies, and dampings, respectively. The following fit values were obtained: $\varepsilon_{Si,\infty} = 12$, $\varepsilon_{SiO_2,\infty} = 2.34$, $S_1 = 0.1$, $S_2 = 0.8$, $\nu_1 = 806$ cm$^{-1}$, $\nu_2 = 1078$ cm$^{-1}$, $\Gamma_1 = 63$ cm$^{-1}$, and $\Gamma_2 = 31$ cm$^{-1}$. For the screened plasma frequency and damping, the following values were obtained: $\nu_p = 2400$ cm$^{-1}$ and $\Gamma_p = 410$ cm$^{-1}$, respectively.

The dielectric function of ML-hBN was obtained by fitting the reflection spectra of the ML-hBN layer on $SiO_2/Si$. The sample was modeled as a 6 nm-thick ML-hBN (thickness measured by AFM, Figure 1b) on a 285 nm-thick $SiO_2$ layer on a semi-infinite bulk Si, which was described with the dielectric functions provided above. The optical anisotropy of ML-hBN was considered by defining a dielectric tensor with an in-plane component is described by a Lorenz oscillator according to:

$$\varepsilon_\perp(\nu) = \varepsilon_{\perp,\infty} + \varepsilon_{\perp,\infty} \frac{\nu_{\perp,LO}^2 - \nu_{\perp,TO}^2}{\nu_{\perp,TO}^2 - \nu^2 - i\nu\Gamma_\perp} \tag{5}$$

The out-of-plane dielectric value  was fixed to $\varepsilon_{\parallel,\infty} = 2.95$ (as reported by Giles et al.[28]). Fitting the reflection spectrum yielded the in-plane high-frequency permittivity, $\varepsilon_{\perp,\infty} = 4.7$, transverse optical phonon frequency, $\nu_{\perp,TO} = 1369$ cm$^{-1}$, longitudinal phonon frequency, $\nu_{\perp,LO} = 1621$ cm$^{-1}$ and damping, $\Gamma_\perp = 19$ cm$^{-1}$.

*Scattering-Type Scanning Near-Field Optical Microscopy (s-SNOM)*:  A commercial s-SNOM setup (neaSNOM, Attocube AG) was used. A Pt/Ir-coated atomic force microscopy tip, with a curvature radius $a \approx 25$ nm, (Arrow-NCPt-50, NanoWorld AG) was illuminated by p-polarized infrared radiation generated by a tunable quantum cascade lasers (QCL, Daylight Solutions) with an average power of $\approx$3 mW. The tip-scattered field was detected with a pseudo-heterodyne interferometric module. To suppress background scattering, the tip was oscillating at a frequency $\Omega \cong 270$ kHz and the interferometric detector signal was demodulated at a frequency $3\Omega$, yielding near-field amplitude and phase signals, $s_3$ and $\varphi_3$, respectively.

*Simulation of s-SNOM Images of Figure 3h*:  An analytical model was developed to simulate near-field images (Figure 2g,h) and to analyze their FTs (Figure 3a). The s-SNOM tip was modeled as a point dipole, which: i) excites PhPs that propagate along the ML-hBN with wavevector $k_p$ and ii) scatters (into free-space radiation) the PhPs that are backscattered by the defects in the ML-hBN. Each defect (enumerated by $j$) was modeled as a point scatter with a polarizability $\alpha_j$. First-order perturbation theory was applied by considering that the defects interact only with the PhPs launched by the tip, but not with PhPs that scatter at the defects. The

z-component of the total PhP field scattered by the tip at position $r = (x,y)$ was obtained according to

$$\Delta E_z(r) \propto \sum_j \alpha_j \frac{e^{2ik_p|\mathbf{r}-\mathbf{r_j}|}}{|\mathbf{r}-\mathbf{r_j}|} \tag{6}$$

where $r_j$ is the position of the $j$-th defect, and the summation is carried out over all defects. FT of Equation (6) yields Equation (1) of the main text (for more details, see the Supporting Information). It is noted that in the s-SNOM experiments, there is an additional tip-scattered field, which originates from the tip-sample near-field interaction induced by the incident field, $E_{z,0}(r)$.[44] Considering, in first approximation, that spatial variations of this near-field interaction are negligible compared to the spatial signal variations caused by PhP scattering, it was set $E_{z,0}(r) = E_{z,0} = const.$ can be set. The simulated images shown in Figure 2h of the main text were subsequently obtained according to:

$$\sigma(x,y) = s(x,y)e^{i\varphi(x,y)} = E_{z,0} + \Delta E_z(x,y) \tag{7}$$

where $E_{z,0}$ is set to a value larger than the maximum of $|\Delta E_z(x,y)|$.

*Fourier Transform of Measured and Simulated Complex-Valued s-SNOM Images*: The squared modulus of 2D Fourier transform of the complex-valued signal $\sigma(x,y) = s(x,y)e^{i\varphi(x,y)}$ was calculated, with $s(x,y)$ and $\varphi(x,y)$ being the s-SNOM amplitude and phase images, according to

$$\left|\hat{\sigma}(k_x,k_y)\right|^2 = \left|\iint dxdy\, H(x,y)\sigma(x,y)e^{-2\pi i\left(k_x x + k_y y\right)}\right|^2 \tag{8}$$

where $H(x,y)$ is the Hann window function[45] used to reduce artifacts due to the finite size of the images. Radial profiles of $\hat{\sigma}$ were obtained by calculating the angular average of $|\hat{\sigma}(k_x,k_y)|^2$ at a given distance $k = \sqrt{k_x^2 + k_y^2}$ from the origin.

*Calculation of PhP Dispersion, Propagation Length, and Lifetime*: To calculate the PhP dispersion $\nu(k_p')$, propagation length $L_p = 1/k_p''$, and lifetime $\tau_{field} = L_p/\nu_g$ with group velocity $\nu_g = d\omega/dk_p'$, the complex-valued wavevector $k_p = k_p' + ik_p''$ was determined from the calculated complex-valued Fresnel reflection coefficient $r_p$ of the ML-hBN/SiO$_2$/Si samples by employing the multilayer transfer matrix approach.[46] To that end, the poles of $r_p(k_p' + ik_p'',\nu)$ were determined by solving numerically the equation $1/\text{Abs}(r_p) = 0$. For ML-hBN, SiO$_2$ and Si the dielectric functions obtained by fitting the far-field reflection spectra as described above were used.

*Fabrication of ML-hBN Ribbons*: Arrays of ML-hBN ribbons (Figure 4) were fabricated by high-resolution electron beam lithography (EBL, Raith 150TWO). First, PMMA was spin-coated onto the ML-hBN on the SiO$_2$/Si substrates. Second, a 2 nm-thick Au layer was sputtered onto the e-beam resist as a conductive layer to avoid charging. Ribbon arrays with a size of $60 \times 60\ \mu m^2$ were patterned by EBL within homogenous areas of the ML-hBNs, which were identified by optical inspection with a light microscope. The conductive layer was removed after e-beam exposure by immersing the sample in Au etchant for 10 s, followed by rinsing in water and IPA. The sample was then developed in MIBK(methyl isobutyl ketone):IPA (3:1) and rinsed in IPA. In the following, a hard mask to protect the ML-hBN during the etching process was fabricated by e-beam evaporation of 3 nm of Cr and thermal evaporation of 50 nm Al layer in an ultrahigh vacuum. Lift-off in acetone yielded a structured hard metal mask on the ML-hBN. The uncovered ML-hBN areas were removed by reactive ion etching (Oxford Plasmalab 80 Plus) using a 20 sccm SF$_6$/Ar 1:1 flow and a 100 W plasma power at 100 mTorr pressure for 40 s. The Cr/Al hard mask was chemically etched using a Cr etchant solution and rinsed in DI water. Finally, the sample was cleaned by rinsing it in IPA and drying it with a N$_2$ gun.

*Fitting of the Far-Field FTIR Reflection Spectra of hBN Ribbons*: The reflection spectra of the ML-hBN ribbons arrays (Figure 4b,c) exhibit an asymmetric lineshape, owing to the interference between the radiation re-

flected at the SiO$_2$/Si substrate and that scattered by the ML-hBN ribbons. To extract the spectral resonance positions, $\nu_{res}$, and the linewidths, $\Delta\nu$, of the PhP resonances, a Fano fit was performed to the measured and simulated reflection spectra according to:[47]

$$R(\nu) \propto \frac{(\varepsilon + q)^2}{(1 + \varepsilon^2)} \tag{9}$$

where $q$ is the Fano parameter and $\varepsilon = 2(\nu - \nu_{res})/\Delta\nu$.

*Simulation of ML-hBN Ribbon Arrays Reflection Spectra*: The reflection spectra of ribbon arrays on the SiO$_2$/Si substrate (Figure 4c) were obtained by full-wave numerical simulations using the finite-elements method in the frequency domain (COMSOL Multiphysics). The dielectric functions obtained from fitting the far-field reflection spectra of hBN, SiO$_2$, and Si were used. A semi-infinite Si substrate with 285 nm SiO$_2$ on top was assumed. The ML-hBN thickness and ribbon width are provided in Figure 4c.

## Supporting Information

Supporting Information is available from the Wiley Online Library or from the author.

## Acknowledgements

## Conflict of Interest

R.H. was a co-founder of Neaspec GmbH, which now is a part of Attocube AG, a company producing s-SNOM systems, such as the one used in this study. The remaining authors declare no competing interests.

## Data Availability Statement

The data that support the findings of this study are available from the corresponding author upon reasonable request.

## Keywords

[1] D. N. Basov, M. M. Fogler, F. J. García de Abajo, *Science* **2016**, *354*, aag1992.

[2] T. Low, A. Chaves, J. D. Caldwell, A. Kumar, N. X. Fang, P. Avouris, T. F. Heinz, F. Guinea, L. Martin-Moreno, F. Koppens, *Nat. Mater.* **2017**, *16*, 182.

[3] G. X. Ni, A. S. McLeod, Z. Sun, L. Wang, L. Xiong, K. W. Post, S. S. Sunku, B.-Y. Jiang, J. Hone, C. R. Dean, M. M. Fogler, D. N. Basov, *Nature* **2018**, *557*, 530.

[4] S. Dai, Z. Fei, Q. Ma, A. S. Rodin, M. Wagner, A. S. McLeod, M. K. Liu, W. Gannett, W. Regan, K. Watanabe, T. Taniguchi, M. Thiemens, G. Dominguez, A. H. Castro Neto, A. Zettl, F. Keilmann, P. Jarillo-Herrero, M. M. Fogler, D. N. Basov, *Science* **2014**, *343*, 1125.

[5] W. Ma, P. Alonso-González, S. Li, A. Y. Nikitin, J. Yuan, J. Martín-Sánchez, J. Taboada-Gutiérrez, I. Amenabar, P. Li, S. Vélez, C. Tollan, Z. Dai, Y. Zhang, S. Sriram, K. Kalantar-Zadeh, S.-T. Lee, R. Hillenbrand, Q. Bao, *Nature* **2018**, *562*, 557.

[6] J. Taboada-Gutiérrez, G. Álvarez-Pérez, J. Duan, W. Ma, K. Crowley, I. Prieto, A. Bylinkin, M. Autore, H. Volkova, K. Kimura, T. Kimura, M.-H. Berger, S. Li, Q. Bao, X. P. A. Gao, I. Errea, A. Y. Nikitin, R. Hillenbrand, J. Martín-Sánchez, P. Alonso-González, *Nat. Mater.* **2020**, *19*, 964.

[7] Q. Zhang, G. Hu, W. Ma, P. Li, A. Krasnok, R. Hillenbrand, A. Alù, C.-W. Qiu, *Nature* **2021**, *597*, 187.

[8] D. Rodrigo, O. Limaj, D. Janner, D. Etezadi, F. J. García de Abajo, V. Pruneri, H. Altug, *Science* **2015**, *349*, 165.

[9] M. Autore, P. Li, I. Dolado, F. J. Alfaro-Mozaz, R. Esteban, A. Atxabal, F. Casanova, L. E. Hueso, P. Alonso-González, J. Aizpurua, A. Y. Nikitin, S. Vélez, R. Hillenbrand, *Light Sci. Appl.* **2018**, *7*, 17172.

[10] M. Autore, I. Dolado, P. Li, R. Esteban, F. J. Alfaro-Mozaz, A. Atxabal, S. Liu, J. H. Edgar, S. Vélez, F. Casanova, L. E. Hueso, J. Aizpurua, R. Hillenbrand, *Adv. Opt. Mater.* **2021**, *9*, 2001958.

[11] F. J. Alfaro-Mozaz, P. Alonso-González, S. Vélez, I. Dolado, M. Autore, S. Mastel, F. Casanova, L. E. Hueso, P. Li, A. Y. Nikitin, R. Hillenbrand, *Nat. Commun.* **2017**, *8*, 15624.

[12] I. Dolado, F. J. Alfaro-Mozaz, P. Li, E. Nikulina, A. Bylinkin, S. Liu, J. H. Edgar, F. Casanova, L. E. Hueso, P. Alonso-González, S. Vélez, A. Y. Nikitin, R. Hillenbrand, *Adv. Mater.* **2020**, *32*, 1906530.

[13] P. Pons-Valencia, F. J. Alfaro-Mozaz, M. M. Wiecha, V. Biolek, I. Dolado, S. Vélez, P. Li, P. Alonso-González, F. Casanova, L. E. Hueso, L. Martín-Moreno, R. Hillenbrand, A. Y. Nikitin, *Nat. Commun.* **2019**, *10*, 3242.

[14] E. J. C. Dias, R. Yu, F. J. García de Abajo, *Light Sci. Appl.* **2020**, *9*, 87.

[15] Y. Wu, J. Ordonez-Miranda, S. Gluchko, R. Anufriev, D. D. S. Meneses, L. Del Campo, S. Volz, M. Nomura, *Sci. Adv.* **2020**, *6*, eabb4461.

[16] X. Li, W. Cai, J. An, S. Kim, J. Nah, D. Yang, R. Piner, A. Velamakanni, I. Jung, E. Tutuc, S. K. Banerjee, L. Colombo, R. S. Ruoff, *Science* **2009**, *324*, 1312.

[17] N. J. Bareza, K. K. Gopalan, R. Alani, B. Paulillo, V. Pruneri, *ACS Photonics* **2020**, *7*, 879.

[18] H. Hu, X. Yang, X. Guo, K. Khaliji, S. R. Biswas, F. J. García de Abajo, T. Low, Z. Sun, Q. Dai, *Nat. Commun.* **2019**, *10*, 1131.

[19] F. H. L. Koppens, T. Mueller, P. Avouris, A. C. Ferrari, M. S. Vitiello, M. Polini, *Nat. Nanotechnol.* **2014**, *9*, 780.

[20] S.-J. Yu, S. Jiang, J. A. Roberts, M. A. Huber, H. Yao, X. Shi, H. A. Bechtel, S. N. G. Corder, T. F. Heinz, X. Zheng, J. A. Fan, *ACS Nano* **2022**, *16*, 3027.

[21] A. Mancini, L. Nan, F. J. Wendisch, R. Berté, H. Ren, E. Cortés, S. A. Maier, *ACS Photonics* **2022**, *9*, 3696.

[22] C. Ashworth, *Nat. Rev. Phys.* **2020**, *2*, 176.

[23] T.-A. Chen, C.-P. Chuu, C.-C. Tseng, C.-K. Wen, H.-S. P. Wong, S. Pan, R. Li, T.-A. Chao, W.-C. Chueh, Y. Zhang, Q. Fu, B. I. Yakobson, W.-H. Chang, L.-J. Li, *Nature* **2020**, *579*, 219.

[24] K. Y. Ma, L. Zhang, S. Jin, Y. Wang, S. I. Yoon, H. Hwang, J. Oh, D. S. Jeong, M. Wang, S. Chatterjee, G. Kim, A.-R. Jang, J. Yang, S. Ryu, H. Y. Jeong, R. S. Ruoff, M. Chhowalla, F. Ding, H. S. Shin, *Nature* **2022**, *606*, 88.

[25] S. Dai, S. Fang, N. Rivera, Y. Stehle, B. Jiang, J. Shen, R. Y. Tay, C. J. Ciccarino, Q. Ma, D. Rodan-Legrain, P. Jarillo-Herrero, E. H. T. Teo, M. M. Fogler, P. Narang, J. Kong, D. N. Basov, *Adv. Mater.* **2019**, *31*, 1806603.

[26] S. Reich, A. C. Ferrari, R. Arenal, A. Loiseau, I. Bello, J. Robertson, *Phys. Rev. B* **2005**, *71*, 205201.

[27] R. V. Gorbachev, I. Riaz, R. R. Nair, R. Jalil, L. Britnell, B. D. Belle, E. W. Hill, K. S. Novoselov, K. Watanabe, T. Taniguchi, A. K. Geim, P. Blake, *Small* **2011**, *7*, 465.

[28] A. J. Giles, S. Dai, I. Vurgaftman, T. Hoffman, S. Liu, L. Lindsay, C. T. Ellis, N. Assefa, I. Chatzakis, T. L. Reinecke, J. G. Tischler, M. M. Fogler, J. H. Edgar, D. N. Basov, J. D. Caldwell, *Nat. Mater.* **2018**, *17*, 134.

[29] E. Y. Ma, J. Hu, L. Waldecker, K. Watanabe, T. Taniguchi, F. Liu, T. F. Heinz, *Nano Lett.* **2022**, *22*, 8389.

[30] N. Ocelic, A. Huber, R. Hillenbrand, *Appl. Phys. Lett.* **2006**, *89*, 101124.

[31] Z. Zheng, J. Chen, Y. Wang, X. Wang, X. Chen, P. Liu, J. Xu, W. Xie, H. Chen, S. Deng, N. Xu, *Adv. Mater.* **2018**, *30*, 1705318.

[32] A. Bylinkin, M. Schnell, M. Autore, F. Calavalle, P. Li, J. Taboada-Gutiérrez, S. Liu, J. H. Edgar, F. Casanova, L. E. Hueso, P. Alonso-Gonzalez, A. Y. Nikitin, R. Hillenbrand, *Nat. Photonics* **2021**, *15*, 197.

[33] S. Chen, A. Bylinkin, Z. Wang, M. Schnell, G. Chandan, P. Li, A. Y. Nikitin, S. Law, R. Hillenbrand, *Nat. Commun.* **2022**, *13*, 1374.

[34] J. S. Gomez-Diaz, M. Tymchenko, A. Alù, *Phys. Rev. Lett.* **2015**, *114*, 233901.

[35] S. A. Maier, in *World Scientific Handbook of Metamaterials Plasmonics*, vol. *4*, World Scientific Publishing, Singapore **2018**, pp. 307–338.

[36] N. J. Bareza, B. Paulillo, T. M. Slipchenko, M. Autore, I. Dolado, S. Liu, J. H. Edgar, S. Vélez, L. Martín-Moreno, R. Hillenbrand, V. Pruneri, *ACS Photonics* **2022**, *9*, 34.

[37] L. Novotny, B. Hecht, *Principles of Nano-Optics*, Cambridge University Press, Cambridge, UK, **2012**.

[38] E. Yoxall, M. Schnell, A. Y. Nikitin, O. Txoperena, A. Woessner, M. B. Lundeberg, F. Casanova, L. E. Hueso, F. H. L. Koppens, R. Hillenbrand, *Nat. Photonics* **2015**, *9*, 674.

[39] X. Chen, Z. Yao, S. Xu, A. S. McLeod, S. N. Gilbert Corder, Y. Zhao, M. Tsuneto, H. A. Bechtel, M. C. Martin, G. L. Carr, M. M. Fogler, S. G. Stanciu, D. N. Basov, M. Liu, *ACS Photonics* **2021**, *8*, 2987.

[40] X. Chen, S. Xu, S. Shabani, Y. Zhao, M. Fu, A. J. Millis, M. M. Fogler, A. N. Pasupathy, M. Liu, D. N. Basov, *Adv. Mater.* **2022**, 2109171.

[41] S. Xu, A. S. McLeod, X. Chen, D. J. Rizzo, B. S. Jessen, Z. Yao, Z. Wang, Z. Sun, S. Shabani, A. N. Pasupathy, A. J. Millis, C. R. Dean, J. C. Hone, M. Liu, D. N. Basov, *ACS Nano* **2021**, *15*, 18182.

[42] S. Castilla, I. Vangelidis, V.-V. Pusapati, J. Goldstein, M. Autore, T. Slipchenko, K. Rajendran, S. Kim, K. Watanabe, T. Taniguchi, L. Martín-Moreno, D. Englund, K.-J. Tielrooij, R. Hillenbrand, E. Lidorikis, F. H. L. Koppens, *Nat. Commun.* **2020**, *11*, 4872.

[43] M. Dressel, G. Grüner, *Electrodynamics of Solids: Optical Properties of Electrons in Matter*, Cambridge University Press, Cambridge, UK, **2002**.

[44] E. Yoxall, M. Schnell, S. Mastel, R. Hillenbrand, *Opt. Express* **2015**, *23*, 13358.

[45] F. J. Harris, *Proc. IEEE* **1978**, *66*, 51.

[46] N. C. Passler, A. Paarmann, *J. Opt. Soc. Am. B* **2017**, *34*, 2128.

[47] V. Giannini, Y. Francescato, H. Amrania, C. C. Phillips, S. A. Maier, *Nano Lett.* **2011**, *11*, 2835.